CEAS Aeronautical Journal (2023) 14:661–677
https://doi.org/10.1007/s13272-023-00674-x

ORIGINAL PAPER

Nonlinear system identification of a UAV model with distributed aerodynamics and flexible structure

Benjamin Herrmann[1] · **Julian Theis**[1] · **Frank Thielecke**[1]

Received: 27 February 2023 / Revised: 8 June 2023 / Accepted: 26 June 2023 / Published online: 25 July 2023

Abstract

This paper presents the nonlinear system identification of a slightly flexible 25 kg fixed-wing UAV in the time-domain using a computationally efficient distributed aerodynamics model and a linear structural dynamics representation. The equations of motion are formed by making use of the free vibration modes of the structure and the mean axes formulation. The structural modes and mode shapes are determined from ground vibration tests. The distributed aerodynamics, accounting for elastic deformations, are modeled using a quasi-steady stability and control derivative approach and by applying strip theory. Initial distributions for the derivatives are obtained from vortex-lattice-method calculations. For matching the model response to the measured response, parameters for scaling the initial derivative distributions are introduced. The flexible model is subsequently identified based on flight test data using the output error method in the time-domain and maximum-likelihood estimation. A good overall identification result is achieved with a close match of the fast aircraft dynamics. Finally, an evaluation is given on the suitability of the identified model for real-time simulation, loads' estimation, and active load control law design.

Keywords Nonlinear system identification · Aeroelastic modeling · UAV · Flight tests

List of symbols

a_x, a_y, a_z	Translational accelerations expressed in O_{B^R} coordinates, m/s^2
$\boldsymbol{b}_{cm}$	Position vector of O_{B^G} relative to O_{B^R} to, m
$\boldsymbol{b}_{NP}$	Position vector of neutral point relative to O_{B^G}, m
$\boldsymbol{b}_{r,NP}$	Rigid-body position vector of neutral point relative to O_{B^G}, m
$\boldsymbol{b}_{r,SP}$	Rigid-body position vector of structure support point relative to O_{B^G}, m
$\boldsymbol{C}^{A,F}$	Coefficient vector of aerodynamic forces
$\boldsymbol{C}^{A,M}$	Coefficient vector of aerodynamic moments
C_D	Drag coefficient
C_{D_0}	Zero drag coefficient
C_l	Roll moment coefficient
C_{l_0}	Zero roll moment coefficient
C_L	Lift coefficient
C_{L_0}	Zero lift coefficient
$C_{L_{\alpha,\varphi=0}}$	Lift curve slope of unswept wing, 1/rad
$C_{L_{\delta_c}}$	Lift stability derivative of control surfaces, 1/rad
C_m	Pitch moment coefficient
C_{m_0}	Zero pitch moment coefficient
C_n	Yaw moment coefficient
C_Y	Side force coefficient
C_{Y_β}	Side force stability derivative, 1/rad
$C_{Y_{\delta_r}}$	Side force rudder control derivative, 1/rad
$\overline{c}$	Wing aerodynamic mean chord, m
c_i	Local strip chord, m
$\boldsymbol{D}$	Diagonal matrix with entries $\{\overline{s}, \overline{c}, \overline{s}\}$, m
$\boldsymbol{d}$	Elastic (translational) deformation vector in O_{B^R} coordinates, m
$\mathrm{d}V$	Volume element, m^3
y	Local strip width, m
$\boldsymbol{F}^A$	Vector of aerodynamic forces, N
$\boldsymbol{F}^{ext}$	Vector of external forces, N
$\boldsymbol{F}_{\mathrm{MP}}$	Vector of forces and moments at mass point, N and N·m
$\boldsymbol{F}_{\mathrm{SG}}$	Vector of internal loads at strain gauge, N and N·m

---

✉ Benjamin Herrmann
benjamin.herrmann@tuhh.de

Julian Theis
julian.theis@tuhh.de

Frank Thielecke
frank.thielecke@tuhh.de

[1] Institute of Aircraft Systems Engineering, Hamburg University of Technology, Nesspriel 5, 21129 Hamburg, Germany

$\boldsymbol{G}$	Gravity acceleration vector, m/s^2
h	Altitude, m
$\boldsymbol{J}$	Inertia tensor, kg·m^2
k	K-factor of induced drag
k_C	Scaling parameter for derivative distribution
$\boldsymbol{M}^A$	Vector of aerodynamic moments, N·m
$\boldsymbol{M}^{ext}$	Vector of external moments, N·m
m	Aircraft mass, kg
N	Number of samples
n_e	Number of elastic modes
n_f	Number of flaperons
n_s	Number of strips
O_{A^S}	Local aerodynamic strip frame
O_{B^G}	Global body-fixed frame
O_{B^R}	Body-reference frame (center of mass)
O_{B^S}	Local strip-fixed frame
$O_{B^{SG}}$	Strain gauge sensor frame
O_I	Inertial reference frame
$\boldsymbol{p}$	Position vector of mass element relative to O_{B^R}, m
p, q, r	Angular rates (roll, pitch, yaw), rad/s
p_s	Static pressure, Pa
$\overline{q}$	Dynamic pressure, Pa
$\overline{q}_A$	Dynamic pressure of relative flow, Pa
$\overline{q}_N$	Dynamic pressure of normal flow, Pa
Q_{η_j}	Generalized forces of j-th mode, N·m
$\boldsymbol{r}$	Position vector of mass element relative to O_I, m
$\boldsymbol{r}_0$	Position vector of origin of O_{B^R}, m
S_i	Local strip surface area, m^2
S_{ref}	Wing reference surface area, m^2
$\overline{s}$	Half wing span, m
$\boldsymbol{s}$	Undeformed position vector relative to O_{B^R}, m
T	Air temperature, deg
$\boldsymbol{T}_{B^R I}$	Transformation matrix from O_I to O_{B^R}
$\boldsymbol{T}_{B^S B^G}$	Transformation matrix from O_{B^G} to O_{B^S}
$\boldsymbol{T}_{B^S B^R}$	Transformation matrix from O_{B^R} to O_{B^S}
$\boldsymbol{T}_{B^{SG} B^R}$	Transformation matrix from O_{B^R} to $O_{B^{SG}}$
$\boldsymbol{T}_{\mathrm{SGMP}}$	Transformation matrix from mass point forces/ moments to strain gauge internal loads
$\boldsymbol{T}_{\varphi}$	Transformation matrix from the undeformed strip to O_{B^S}
t_{init}	Time of initial maneuver condition, s
U_i	Theil's inequality coefficient for i-th output
u, v, w	Translational velocities expressed in O_{B^R} coordinates, m/s
u_I, v_I, w_I	Translational velocities expressed in O_I coordinates, m/s
u_A, v_A, w_A	Translational aerodynamic velocities, m/s
$\boldsymbol{u}$	Input vector
$\boldsymbol{V}$	Translational velocity vector of O_{B^R}, m/s
V_A	Aerodynamic velocity at O_{B^R}, m/s
$\boldsymbol{V}_{A,i}$	Local aerodynamic velocity vector, m/s
$\boldsymbol{V}_{N,i}$	Local normal flow vector, m/s
V_{TAS}	True airspeed, m/s
$\boldsymbol{v}$	Measurement noise vector
X_0	Steady flow-separation point
$\boldsymbol{y}$	System output vector
$\hat{\boldsymbol{y}}$	Simulation model output vector
$\boldsymbol{y}_d$	Deterministic system output vector
α	Angle of attack, rad
α_{eff}	Effective angle of attack, rad
β	Angle of sideslip, rad
β_{eff}	Effective angle of sideslip, rad
Δt_{ϵ_T}	Time delay of downwash at tailplane, s
δ_a	Aileron deflection, rad
δ_c	Control surface deflection, rad
δ_e	Elevator deflection, rad
δ_f	Flaperon deflection, rad
δ_r	Rudder deflection, rad
ϵ_b	Bending strain, 0.01%
ϵ_s	Shear strain, 0.01%
ϵ_t	Torsion strain, 0.01%
ϵ_T	Induced downwash angle, rad
$\varepsilon_0, \varepsilon_e$	Rigid and elastic twist angle, rad
η	Generalized displacement coordinate
λ	Longitude, deg
μ	Generalized mass, kg·m^2
ν_0, ν_e	Rigid and elastic dihedral angle, rad
$\boldsymbol{\omega}$	Angular velocity vector of O_{B^R}, rad/s
$\boldsymbol{\omega}_A$	Aerodynamic angular velocity vector of O_{B^R}, rad/s
ω_n	Undamped natural (modal) frequency, rad/s
ρ	Air density, kg·m^{-3}
ξ	Structural (modal) damping ratio
φ	Latitude, deg
$\boldsymbol{\varphi}$	Elastic angular deformation vector relative to O_{B^R}, rad
φ_e	Elastic sweep angle, rad
φ_{25c}	Rigid sweep angle at quarter chord line, rad
Φ, Θ, Ψ	Euler angles (roll, pitch, yaw), rad
$\boldsymbol{\Phi}_j$	Mode shapes
$\boldsymbol{\Phi}_{\mathrm{ang},j}$	Mode shapes for elastic angular deformation
$\boldsymbol{\Phi}_{\mathrm{trans},j}$	Mode shapes for elastic translational deformation
$\boldsymbol{\Theta}$	Estimation parameter vector
$\boldsymbol{\Theta}_0$	Initial estimation parameter vector
Θ_i	Estimation parameter
$(\cdot)\vert_{B^R}$	$(\cdot)$ expressed in O_{B^R}

1 Introduction

Main drivers in aircraft development, in addition to safety, relate to the need of an increased fuel efficiency to reduce operational cost and fulfill increasingly demanding environmental regulations. The efforts have led to constructing aircraft with lighter structures and higher aspect ratio wings which thus become more flexible. Due to the increase in flexibility, such wings are characterized by lower natural frequencies and exhibit increased in-flight deformations. These can lead to a coupling of rigid-body motion and elastic deformation through the aerodynamic forces and moments [1, 2]. Flight control systems further complicate the interaction, possibly leading to degraded [3] or unstable [4] control performance. Therefore, these interactions need to be considered in the design models for flight control systems.

Depending on the characteristics of the aircraft, the purpose of application, or the availability of experimental data, different modeling frameworks are required. In the context of this work, the objective is the development of an aeroelastic model for a slightly flexible 25 kg fixed-wing UAV that can be adapted based on flight test data using system identification techniques in the time-domain. The model is intended for real-time simulation, loads' estimation, and active load control law design. Therefore, a model of moderate complexity with a limited number of state variables is required. Beyond that, it is desired to maintain a distributed aerodynamics model, such that local forces and moments can be calculated.

An overview of different aerodynamics modeling and system identification activities including applications for flexible aircraft is given in [5]. The modeling of flexible aircraft is suggested with an additional dynamic-pressure-dependent part associated with each stability and control derivative of a classical model structure. However, this approach is only valid provided that the rigid-body and structural frequencies are sufficiently separated. A unified framework for modeling flexible aircraft is presented in [6] and later in [7]. The equations of motion are derived by Lagrange's equation and the principle of virtual work. Further, the authors make use of a modal representation of the structure and the mean axes constraints to minimize inertial coupling between the rigid-body and elastic degrees of freedom (assuming small deformations). The nonlinear equations of motion of the flexible aircraft then simplify and are presented in terms of the nonlinear equations of the rigid-body motion and additional linear differential equations for the modal deflections of the structure. The equations are solely coupled by the aerodynamic forces and moments. The modeling of aerodynamics is further proposed with a quasi-steady stability and control derivative approach and by applying strip theory. Strip theory is a simple method often found in models concerned with the investigation of wake vortex encounter, namely aerodynamic interaction models (AIM) [8–10]. In strip theory, the lifting surfaces of the aircraft are divided into spanwise strips. Each strip is then treated as a two-dimensional airfoil with its local geometric and aerodynamic characteristics. This approach allows for the resolution of local relative flow conditions and the resulting change in force and moment distributions. However, the effects of three-dimensional finite span wing are neglected. Outside aerodynamic interaction models, the application of strip theory is, e.g., found in real-time full-envelope aerodynamic models for small UAVs [11]. The modeling methodology of [6] was further adopted in later works by various authors, in [12] together with quasi-steady strip aerodynamics, and in [13, 14] together with unsteady aerodynamics using modified strip theory [15, 16] to account for the effects of finite span and indicial functions [17, 18]. The work of [12, 13] both aimed at modeling only incremental aerodynamics due to elastic deformations, assuming the availability of a rigid-body flight mechanics and aerodynamics model. System identification techniques for flexible aircraft in combination with the framework of [6, 7] can be found in [19, 20] for the identification of a high-performance glider. Although keeping the quasi-steady derivative approach for modeling the aerodynamic forces, moments, and generalized loads, the derivatives are not determined by applying strip theory, but directly estimated as parameters within the parameter estimation process. This modeling approach is a the straightforward extension of the traditional rigid-body approach to a flexible structure, which can be easily combined with system identification techniques. However, the distributed property of the aerodynamics model is lost. Other applications of system identification for flexible aircraft are found, e.g., in [21] for the in-flight identification of structural modes using an eigensystem realization algorithm (ERA).

Given the review on the literature, the framework of [6, 7] is a powerful method for modeling slightly flexible aircraft. Further, strip theory is simple yet effective for modeling local aerodynamic forces and moments. The objective of this work is to maintain this strip aerodynamics model while allowing for the adaption of the model using system identification techniques in the time-domain. The paper is structured as follows. Section 2 introduces the slightly flexible unmanned test aircraft G-Flights Dimona and summarizes the test activities that were performed. Section 3 describes the modeling of the test aircraft. Within this section, the equations of motion are developed using the free vibration modes of the structure and the mean axes formulation of [6]. Further, the modeling of quasi-steady strip aerodynamics is explained. Finally, Sect. 4 presents the identification and evaluation of the flexible model.

2 Unmanned test aircraft G-Flights Dimona

The slightly flexible test aircraft G-Flights Dimona, depicted in Fig. 1, is an unmanned replica of the *HK36 Super Dimona* at a scale of 1:3. It is driven by an electrical motor with a maximum power of 4kW, and has a total mass of 25 kg and a

Fig. 1 Test aircraft G-Flights Dimona

length of 2.4 m. The original wings of the aircraft have been replaced by custom spar, rib, and foil manufactured wings with increased span and flexibility. The total wingspan of the aircraft is 5.4 m with a total wing surface area of 1.68 m^2. The aircraft can either be controlled by a safety pilot via remote control or by a flight control computer. It is equipped with a total of four control surfaces at the trailing edge of each wing: inner/outer ailerons and inner/outer flaperons, which are used for lateral–directional control and for load control. The aircraft further comprises a rudder for lateral–directional control and two elevators for longitudinal control and load control.

2.1 Test instrumentation

The aircraft is equipped with the standard test instrumentation of a rigid-body aircraft and an additional test instrumentation integrated into the structure of fuselage, wings, and empennage. The standard test instrumentation comprises several sensors, computers, and radio equipment. An industry-grade high-precision inertial navigation platform (INS) supported by dual antennas is used for the measurement of GPS position, attitude, velocities, and accelerations. An increased position accuracy of 0.02 m is achieved with a third antenna on ground providing differential GPS correction. Airspeed, angle of attack, angle of sideslip, static air pressure, and air temperature are measured by three air data systems (ADS). They each consist of a five-hole-probe with an additional inertial measurement unit (IMU) and temperature sensor for measurement correction. The airdata systems are located at the left (ADS1) and the right (ADS2) wing as well as at the vertical tail (ADS3). The air data systems were developed in-house and calibrated in wind tunnel experiments [22]. The standard test instrumentation is completed by a data recorder computer and separate real-time flight control computer. The flight control computer serves as the main host for GNC applications and issues control outputs to the servo actuators. Further, it supports direct code deployment from MATLAB/SIMULINK. Data distribution between the sensors and computers is implemented via Ethernet-network and Controller Area Network (CAN). Table 1 lists the available measurement parameters of the standard test instrumentation.

Table 1 Standard measurement parameters

Name	Symbol	Unit
Latitude	φ	deg
Longitude	λ	deg
Altitude	h	m
Roll angle	Φ	rad
Pitch angle	Θ	rad
Heading	Ψ	rad
Roll rate	p^{INS}	rad/s
Pitch rate	q^{INS}	rad/s
Yaw rate	r^{INS}	rad/s
Longitudinal velocity	u_g^{INS}	m/s
Lateral velocity	v_g^{INS}	m/s
Vertical velocity	w_g^{INS}	m/s
Longitudinal acceleration	a_x^{INS}	m/s^2
Lateral acceleration	a_y^{INS}	m/s^2
Vertical acceleration	a_z^{INS}	m/s^2
Angle of attack	$\alpha^{\mathrm{ADS1\text{-}3}}$	deg
Angle of sideslip	$\beta^{\mathrm{ADS1\text{-}3}}$	deg
Static pressure	$p_s^{\mathrm{ADS1\text{-}3}}$	Pa
Dynamic pressure	$\overline{q}^{\mathrm{ADS1\text{-}3}}$	Pa
Air temperature	$T^{\mathrm{ADS1\text{-}3}}$	°C

The additional test instrumentation is distributed at various sections along the fuselage, wings, and empennage to measure structural dynamics and loads. It comprises several IMUs and strain gauges (shear, bending, and torsion) which are concentrated in load measurement stations (LMS). Figure 2 displays the distribution of the sensors along the test aircraft. Since the measurement of loads and structural dynamics for wings and empannage is of prime importance, most sensors are located in these areas.

2.2 Ground vibration test and modal analysis

Considering the slight flexibility of the test aircraft, the assumption of linear structural dynamics is reasonable. Therefore, it was decided to represent the elastic deformation of the structure by a set of free vibration modes and mode shapes. To determine the structural modes of the aircraft, a ground vibration test (GVT) and experimental modal analysis was performed at the Technische Universität Berlin. Hammer and shaker inputs were used to excite the structural vibrations of the aircraft. The first seven structural modes up to the first symmetric wing torsion mode were identified and considered for the structural dynamics model. Details on the measurement setup, test execution, and results are presented

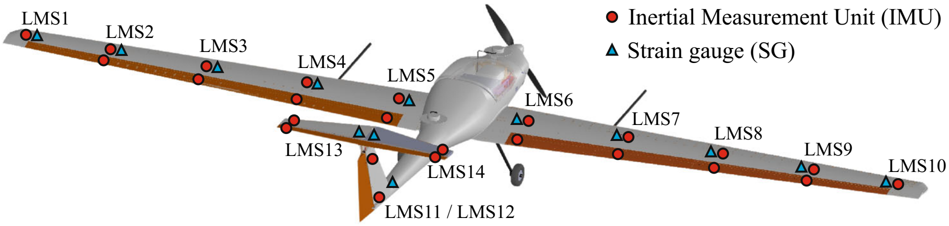

Fig. 2 Distribution of additional test instrumentation along the test aircraft

Table 2 First seven identified structural modes of the G-Flights Dimona

Mode	Definition	Modal frequency ω_n (Hz)	Modal damping ξ (%)
1	First symmetric wing bending	3.97	0.85
2	First antisymmetric wing bending	8.56	1.38
3	First antisymmetric vertical tailplane bending	11.18	1.24
4	First symmetric in-plane wing bending	13.21	1.83
5	Second symmetric wing bending	14.60	1.79
6	First symmetric horizontal tailplane bending	17.24	2.76
7	First symmetric wing torsion	25.83	1.91

in [23]. The structural mode shapes were subsequently determined from a finite-element (FE) model adapted to the GVT data. Table 2 lists the seven structural modes with modal frequency ω_n and modal damping ξ. Figure 3 further visualizes the modes. Especially, the first symmetric wing bending mode exhibits a low natural frequency. Considering the servo actuator bandwidth of 6.74 Hz, it is the mode likely to be excited by control action or atmospheric disturbance.

2.3 Flight tests

A comprehensive flight test campaign was performed to acquire flight data for system identification. The campaign included a total of seven flights with 109 maneuvers performed. All maneuvers were executed with the help of an in-house developed autopilot for aerodynamic parameter identification [24], which was adapted based on an a priori estimation of the rigid-body dynamics. Details on the overall concept and main components of the test setup are given in [25]. A variety of classical maneuvers specifically designed for the identification of the rigid-body dynamics were flown [26]. They comprised multiple longitudinal maneuvers including 3-2-1-1 maneuvers, pulse maneuvers and level deceleration maneuvers. Further, different lateral–directional maneuvers were performed including bank-to-bank maneuvers and rudder doublets. A full description of the maneuver characteristics is presented in [24]. The longitudinal maneuvers were executed by the elevators, while the lateral–directional maneuvers were executed by the ailerons, flaperons, and rudder. To identify the individual control effectiveness of ailerons and flaperons, four different control configurations were varied within the bank-to-bank maneuvers: execution of the maneuvers by (1) inner and outer ailerons, (2) only inner ailerons, (3) only outer ailerons, and (4) inner and outer flaperons. The maneuvers were ultimately repeated around different trim velocities in the range of $V_{TAS} = 18$–$30\,\mathrm{m/s}$.

3 Flexible aircraft model

This section describes the flexible aircraft model. The modeling methodology is based on the framework of [6] and strip theory. The equations of motion are developed by representing the structural dynamics with free vibration modes and making use of the mean axes constraints. The aerodynamic strip forces and moments are modeled using a quasi-steady stability and control derivative approach.

3.1 Equations of motion

The position $\boldsymbol{r}$ of an arbitrary mass element $\rho \mathrm{d}V$ of an elastic body can be expressed in an inertial reference frame O_I (x_I, y_I, z_I) in terms of its relative position $\boldsymbol{p}$ to a body-reference frame O_{BR} (x, y, z) and the position $\boldsymbol{r}_0$ of the origin of O_{BR} (see Fig. 4). The specified positions of the mass element in the inertial and body-reference frames are then related by the expression $\boldsymbol{r} = \boldsymbol{r}_0 + \boldsymbol{p}$. The body-reference axes O_{BR} may rotate with an angular velocity $\boldsymbol{\omega}$ and their orientation may be defined by an arbitrary Euler angle sequence. The axes move with the body but are not necessarily attached to a material point.

Fig. 3 Visualization of the first seven structural modes of the G-Flights Dimona

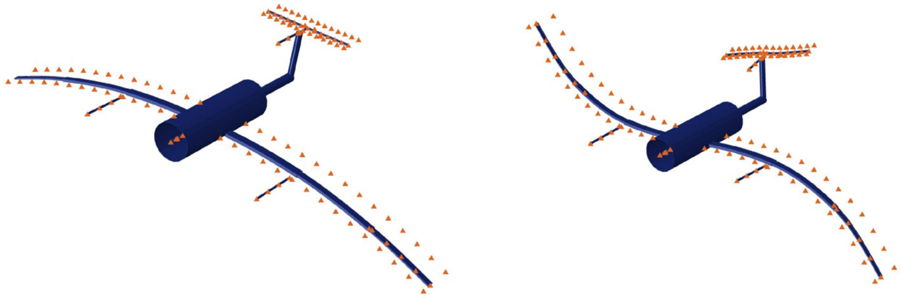

Mode 1, $\omega_n = 3.97$ Hz

Mode 2, $\omega_n = 8.56$ Hz

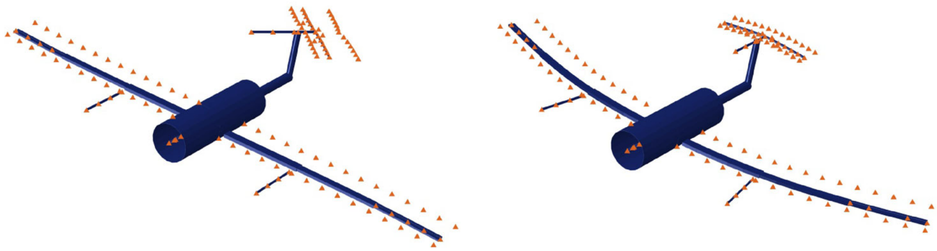

Mode 3, $\omega_n = 11.18$ Hz

Mode 4, $\omega_n = 13.21$ Hz

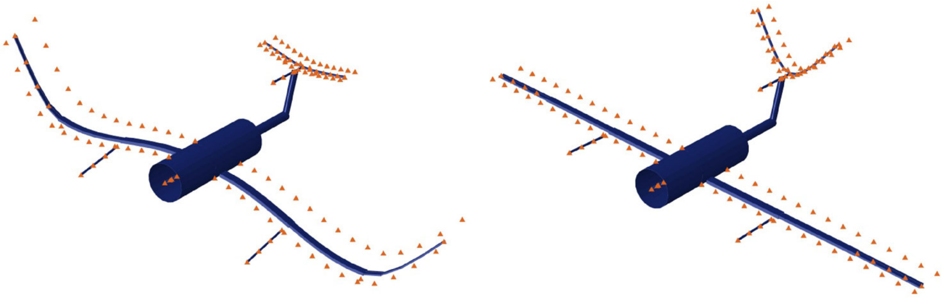

Mode 5, $\omega_n = 14.60$ Hz

Mode 6, $\omega_n = 17.24$ Hz

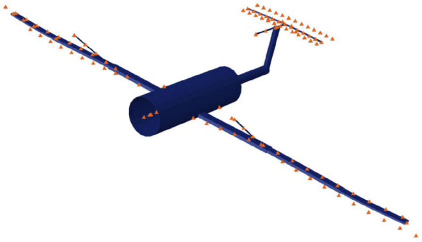

Mode 7, $\omega_n = 25.83$ Hz

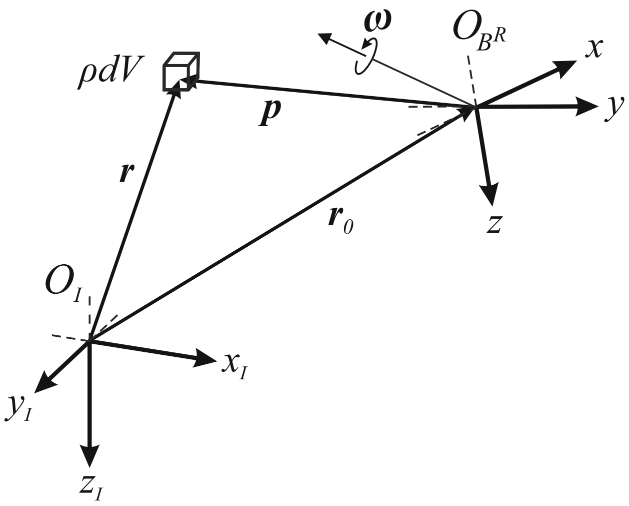

Fig. 4 Definition of a mass element's position using inertial O_I (x_I, y_I, z_I) and body O_{B^R} (x, y, z) reference frames

Assume that a modal description of the structure is available (e.g., from ground vibration tests and finite-element model), such that the elastic deformation $\boldsymbol{d}$ at a point (x, y, z) can be expressed in terms of mode shapes $\boldsymbol{\Phi}_j(x, y, z)$ and the generalized displacement coordinates $\eta_j(t)$ by

$$\boldsymbol{d}(x, y, z, t) = \sum_{j=1}^{n_e} \boldsymbol{\Phi}_j(x, y, z)\eta_j(t), \tag{1}$$

where n_e denotes the number of elastic modes of the unconstrained, undamped vibration problem. Then, the position of the mass element relative to O_{B^R} can be separated into its undeformed part $\boldsymbol{s}(x, y, z)$ (rigid body) and its deformation part $\boldsymbol{d}(x, y, z, t)$. The body-reference frame O_{B^R} may be used to develop the equations of motion of the unconstrained elastic body, assuming that each mass element is treated as a point mass. When doing so, inertial coupling can occur between the rigid degrees of freedom and the elastic degrees of freedom. However, it is found that with a suitable choice of O_{B^R} satisfying the mean axes constraints and the origin of O_{B^R} located at the instantaneous center of mass, the inertial coupling can be neglected [6, 27].

The mean axes, first introduced by [28], define a body frame for which the relative translational and angular momenta, due to the elastic deformation, are zero for all time $t \geq 0$. Combined with the modal description of the structure and only assuming small deformations (i.e., deformation and deformation rate are colinear), the constraints can be expressed by [6, 7]

$$\sum_{j=1}^{n_e} \frac{d\eta_j}{\mathrm{d}t} \int_V \boldsymbol{\Phi}_j \, \rho \, \mathrm{d}V = 0, \sum_{j=1}^{n_e} \frac{d\eta_j}{\mathrm{d}t} \int_V \boldsymbol{s} \times \boldsymbol{\Phi}_j \, \rho \, \mathrm{d}V = 0. \tag{2}$$

It can be shown that for the constraints to be satisfied, the elastic degrees of freedom must be orthogonal to the translational and rotational rigid-body degrees of freedom, respectively [6, 29]. These conditions are guaranteed when the elastic deformations are represented by free vibration modes and the body-reference frame O_{B^R} is located at the instantaneous center of mass. The decoupled equations of motion of the elastic body are then given by [6, 13]

$$\dot{\boldsymbol{V}}|_{B^R} = -\boldsymbol{\omega}|_{B^R} \times \boldsymbol{V}|_{B^R} + \boldsymbol{T}_{B^R I}\boldsymbol{G}\Big|_I + \frac{1}{m}\boldsymbol{F}^{ext}\Big|_{B^R} \tag{3}$$

$$\dot{\boldsymbol{\omega}}|_{B^R} = -\boldsymbol{J}^{-1}(\boldsymbol{\omega}|_{B^R} \times (\boldsymbol{J}\boldsymbol{\omega}|_{B^R})) + \boldsymbol{J}^{-1}\boldsymbol{M}^{ext}|_{B^R} \tag{4}$$

$$\ddot{\eta}_j = -2\xi_j\omega_{n,j}\dot{\eta}_j - \omega_{n,j}^2\eta_j + \frac{1}{\mu_j}Q_{\eta_j}. \tag{5}$$

The first two equations are formally equivalent to the standard nonlinear rigid-body flight dynamic equations for the translational and rotational degrees of freedom. Within these equations, $\boldsymbol{V}|_{B^R}$ and $\boldsymbol{\omega}|_{B^R}$ denote the translational and angular velocity vectors of the body-reference axes O_{B^R} with respect to the inertial reference axes O_I, expressed in body-reference coordinates. The gravity acceleration vector $\boldsymbol{G}|_I$ is expressed in O_I coordinates and transformed to O_{B^R} with the transformation matrix $\boldsymbol{T}_{B^R I}$. The aircraft mass is m and the inertial tensor $\boldsymbol{J}$. Note that with the assumption of small deformations, $\boldsymbol{J}$ is considered constant. The vectors $\boldsymbol{F}^{ext}|_{B^R}$ and $\boldsymbol{M}^{ext}|_{B^R}$ denote the sum of external forces and moments expressed in coordinates of O_{B^R}. Only aerodynamic forces are considered in this work. The last Eq. 5 represents the n_e linear differential equations for the structural dynamics in generalized coordinates. Within these equations, η_j denotes the generalized displacement, $\omega_{n,j}$ the undamped natural frequency, ξ_j the modal damping ratio, μ_j the generalized mass, and Q_{η_j} the generalized forces of each mode. Given the nonlinear rigid-body equations of motion and the linear equations of motion of the structure decoupled as presented, a coupling is solely due to $\boldsymbol{F}^{ext}|_{B^R}$, $\boldsymbol{M}^{ext}|_{B^R}$, and Q_{η_j}.

3.2 Quasi-steady strip aerodynamics

The aerodynamic forces and moments of the test aircraft are modeled by applying strip theory. All effective lifting surfaces, i.e., wings, horizontal tail, and vertical tail, are divided into a finite number of spanwise strips. Each strip is then treated as a two-dimensional airfoil with its own geometric and aerodynamic characteristics. The aerodynamic characteristics are modeled by means of quasi-steady parameters. This implies that the resultant aerodynamic forces and moments at every time instant have reached their steady-state values and are only dependent on the instantaneous configuration and local relative flow. The aerodynamic forces and moments of the fuselage are expressed by additional quasi-steady parameters acting on the center of mass.

Consider the aircraft with its lifting surfaces divided into a finite number of n_s spanwise strips, each with local width $\mathrm{d}y_i$, local chord c_i, and local surface area S_i. Each strip is assigned a structure support point (SP) at its centerline for which the instantaneous deformation (elastic translational deformation and elastic angular deformation) is known from the superposition of structural mode shapes and generalized displacements coordinates. The aircraft can then be treated as a discrete structure of interconnected points, as shown in Fig. 5, which mark the elastic axes of the lifting surfaces.

For the modeling of aerodynamic forces and moments, each strip is further assigned two aerodynamic control points along its centerline, i.e., a neutral point (NP), which is assumed at the 25%-chord position and a zero pressure point (PP0) which is assumed at the 50%-chord position. In strip theory, the strips themselves are assumed non-deformable. Therefore, their motion can be described similar to the motion of a flat plate, as indicated in Fig. 5 for the ith strip.

The instantaneous position of each strip's structure support point, neutral point, and zero pressure point can be described relative to a global body-fixed frame O_{BG}. The frame O_{BG} is aligned with the body-reference axes O_{BR} (origin at the center of mass) but is translated by a vector $\boldsymbol{b}_{cm}$, considered constant due to the assumption of small deformations [7]. Further, a local strip-fixed frame O_{BS} is introduced which defines the instantaneous translation and orientation of the strip's 25%-chord line. Its origin is located at the neutral point and its orientation relative to O_{BG} is defined by three rotations. The three rotation angles are the rigid and elastic dihedral angles ($\nu_{0,i}$, $\nu_{e,i}$), the rigid and elastic twist angles ($\varepsilon_{0,i}$, $\varepsilon_{e,i}$), and the rigid and elastic sweep angles ($\varphi_{25c,i}$, $\varphi_{e,i}$). The rotation from O_{BG} to O_{BS} is given by the transformation matrix $\boldsymbol{T}_{B^S B^G}$. With the alignment of O_{BG} and O_{BR}, the transformation matrix $\boldsymbol{T}_{B^S B^G}$ equals $\boldsymbol{T}_{B^S B^R}$.

Let $\boldsymbol{b}_{NP,i}$ denote the instantaneous position of the strip's neutral point relative to the global body-fixed axes O_{BG}. Further define $\boldsymbol{b}_{r,NP,i}$ as the rigid-body part of the position vector and

$$\boldsymbol{d}(x_i, y_i, z_i, t) = \sum_{j=1}^{n_e} \boldsymbol{\Phi}_{\mathrm{trans},j}(x_i, y_i, z_i)\eta_j(t) \tag{6}$$

$$\boldsymbol{\varphi}(x_i, y_i, z_i, t) = \sum_{j=1}^{n_e} \boldsymbol{\Phi}_{\mathrm{ang},j}(x_i, y_i, z_i)\eta_j(t) \tag{7}$$

as the elastic translational deformation and elastic angular deformation vectors of the ith structure support point along and about the body-reference axes, respectively. In the equations, $\boldsymbol{\Phi}_{\mathrm{trans},j}$ contains the mode shapes for elastic translational deformation and $\boldsymbol{\Phi}_{\mathrm{ang},j}$ the mode shapes for elastic angular deformation. Then, under the assumption of no chord-wise deformation of the strip, the position $\boldsymbol{b}_{NP,i}$ relative to the body-fixed axes O_{BG} is calculated by

$$\begin{aligned}\boldsymbol{b}_{NP,i}(t) &= \boldsymbol{b}_{r,NP,i} + \boldsymbol{d}(x_i, y_i, z_i, t)\\ &\quad + \boldsymbol{T}_{\varphi,i}(t)(\boldsymbol{b}_{r,NP,i} - \boldsymbol{b}_{r,SP,i})\end{aligned} \tag{8}$$

with $\boldsymbol{b}_{r,SP,i}$ denoting the rigid-body position vector of the ith strip structure support point and $\boldsymbol{T}_{\varphi,i}$ denoting the transformation matrix of the rotation about O_{BR} from the undeformed strip to O_{BS} with the angles given by the elastic angular deformation in Eq. 7. Note that $\boldsymbol{b}_{NP,i}$ is indicated time varying to distinguish between the non-time-varying terms in the equation. This notation is omitted for simplification in the following. Similar expressions can be derived for the position vectors of structure support point and zero pressure point.

The aerodynamic characteristics of the strips are modeled with quasi-steady parameters. In this sense, each strip is assigned a local non-dimensional lift coefficient $C_{L,i}$ and a local non-dimensional drag coefficient $C_{D,i}$, where each coefficient itself is formed by stability and control derivatives normalized by ${}^{S_i}/_{S_{\mathrm{ref}}}$

$$\begin{aligned}C_{L,i} &= C_{L_{0,i}} + C_{L_{\alpha,\varphi=0,i}} \cdot \left(\frac{1+\sqrt{X_{0,i}}}{2}\right) \cdot \alpha_{\mathrm{eff},i}\\ &\quad + \sum_{n=1}^{n_c} C_{L_{\delta_{c,n}},i} \cdot \delta_{c,n}\end{aligned} \tag{9}$$

$$C_{D,i} = C_{D_{0,i}} + k_i \cdot C_{L,i}^2. \tag{10}$$

In the equations, $C_{L_{0,i}}$ and $C_{D_{0,i}}$ are the strip's zero lift and drag coefficient, $C_{L_{\alpha,\varphi=0,i}}$ indicates the lift curve slope of the unswept strip, $\alpha_{\mathrm{eff},i}$ is the strip's local effective angle of attack, k_i is the strip's k-factor of induced drag, and $C_{L_{\delta_{c,n}},i}$ and δ_c are the n_c control derivatives and deflections of the available control surfaces, respectively. Steady stall effects are included in terms of Kirchhoff's theory of flow separation and an approximation of the steady flow-separation point $X_{0,i}$ based on hyperbolic tangent [26]. For vertical stabilizer strips, the non-dimensional lift coefficient is interpreted as a side force coefficient $C_{Y,i}$ with the effective angle $\beta_{\mathrm{eff},i}$. All terms are assumed to act on the strip's neutral point, except for $C_{L_{0,i}}$ and $C_{L_{\delta_{c,n}},i} \cdot \delta_{c,n}$, which are assumed to act on the strip's zero pressure point and a variable point along the centerline as a function of the deflection [30], respectively. They are ultimately transferred to the strip's neutral point. The additional moments caused thereby are expressed in terms of non-dimensional moment coefficients $C_{l,i}$ (roll), $C_{m,i}$ (pitch), and $C_{n,i}$ (yaw). Non-dimensionality is achieved through dividing the moments by $\bar{s}$ (roll, yaw) and $\bar{c}$ (pitch), respectively. Finally, the aerodynamic characteristics of the fuselage are modeled by additional non-dimensional force and moment coefficients with classical 1-point stability derivatives.

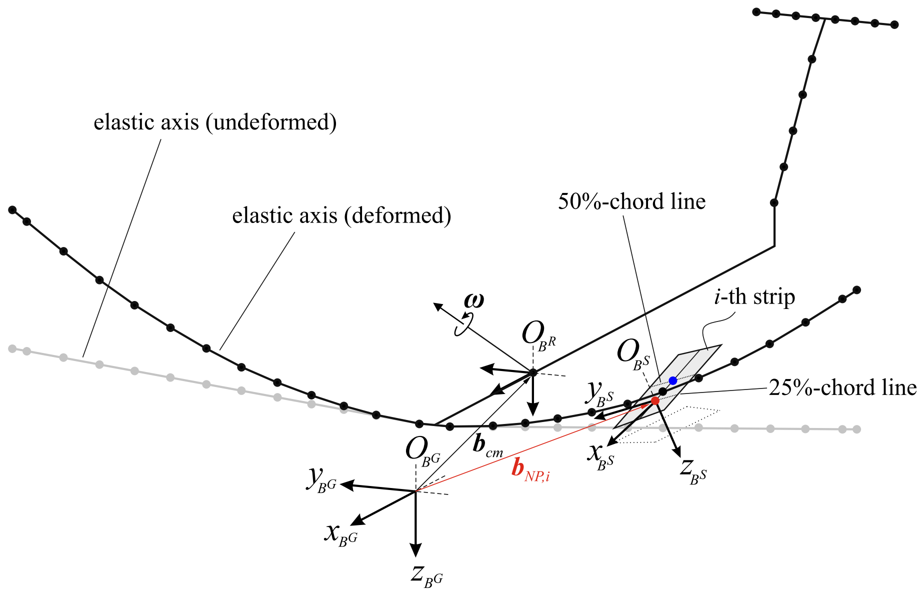

Fig. 5 Position and orientation of the ith strip relative to the global body-fixed frame O_{B^G} and definition of the local strip-fixed frame O_{B^S}

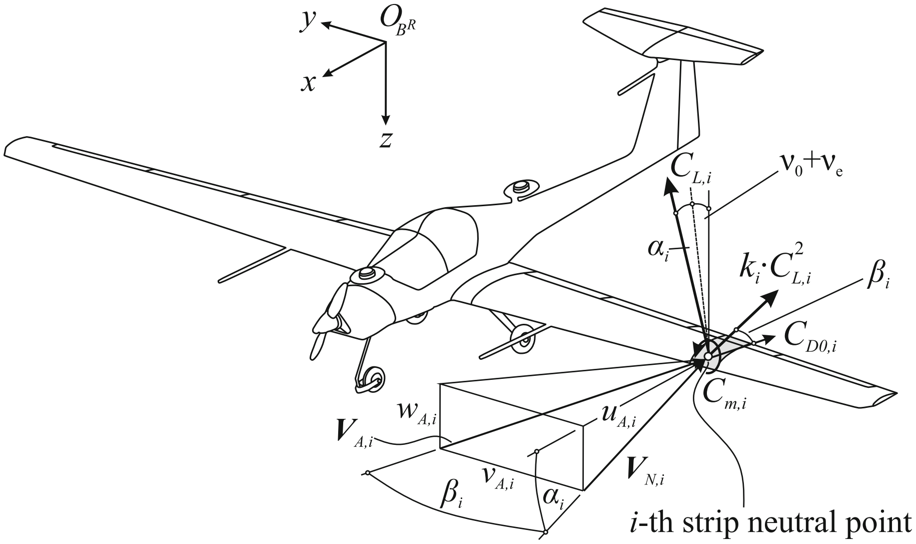

Fig. 6 Local relative flow at the ith strip and force and moment coefficients (assuming $\varphi_{e,i} = 0$)

To calculate the effective angles in Eq. 9, the local relative flow at each strip has to be determined. This is achieved by summing all individual flow components at O_{B^S}, i.e., the linear aerodynamic velocity of O_{B^R}, plus additional terms due to rotation about O_{B^R}, and the velocity of the structure

$$\begin{aligned} \boldsymbol{V}_{A,i}|_{B^R} &= \boldsymbol{V}_A|_{B^R} + \boldsymbol{\omega}_A|_{B^R} \times (\boldsymbol{b}_{NP,i} - \boldsymbol{b}_{cm}) \\ &\quad + \sum_{j=1}^{n_e} \boldsymbol{\Phi}_{\text{trans},j}(x_i, y_i, z_i)\dot{\eta}_j. \end{aligned} \tag{11}$$

The induced velocity due to elastic angular deformation about the structure support point is neglected. In Eq. 11, $\boldsymbol{V}_A|_{B^R}$ and $\boldsymbol{\omega}_A|_{B^R}$ denote the linear and angular aerodynamic velocity vector at O_{B^R}, respectively. Downwash effects are taken into account at tailplane strips by the induced downwash angle $\epsilon_{T,i}$. It is proportional to the angle of attack at O_{B^R} and flaperon deflections, delayed by $\Delta t_{\epsilon_T,i}$, the time the flow requires to reach the tailplane strips [31]

$$\epsilon_{T,i}(t) = \frac{\partial \epsilon_T}{\partial \alpha} \cdot \alpha(t - \Delta t_{\epsilon_T,i}) + \sum_{n=1}^{n_f} \frac{\partial \epsilon_T}{\partial \delta_{f,n}} \cdot \delta_{f,n}(t - \Delta t_{\epsilon_T,i}). \tag{12}$$

Herein, ${}^{\partial \epsilon_T}/_{\partial \alpha}$ and ${}^{\partial \epsilon_T}/_{\partial \delta_{f,n}}$ denote the partial derivatives of the downwash angle to the angle of attack at O_{B^R} and n_f flaperon deflections. In this work, the calculation of $\Delta t_{\epsilon_T,i}$ is simplified by taking the mean distance between wing and horizontal or vertical tail strip neutral points along x_{B^R}, divided by the airspeed V_A at O_{B^R}. The downwash angles are then used to correct the local relative flow at the tailplane strips. The local relative flow is originally defined in the local strip aerodynamic frame O_{A^S}, but as given in Eq. 11, is already expressed in components along O_{B^R}. Then, the angle of attack α_i and angle of sideslip β_i of the local relative flow define the orientation of O_{A^S} relative to O_{B^R}. The local relative flow at the i-th strip is illustrated in Fig. 6.

With the transformation matrix $\boldsymbol{T}_{B^S B^R}$, the local relative flow from Eq. 11 can be expressed in O_{B^S} coordinates. It is then straight forward to calculate the effective angles needed for the calculation of the aerodynamic force coefficient in Eq. 9 from the relative flow components $u_{A,i}$, $v_{A,i}$, and $w_{A,i}$, by

$$\alpha_{\mathrm{eff},i} = \arctan\left(\frac{w_{A,i}|_{B^S}}{u_{A,i}|_{B^S}}\right), \qquad \beta_{\mathrm{eff},i} = \arcsin\left(\frac{v_{A,i}|_{B^S}}{|\boldsymbol{V}_{A,i}|}\right). \tag{13}$$

Indicated in Fig. 6, the orientation of the force and moment coefficients is either given along the coordinates of O_{A^S} (defined by α_i and β_i) or along the normal flow component $\boldsymbol{V}_{N,i}$, but overall rotated about the body-reference axis x_{B^R} by the rigid and elastic dihedral angle.[1] They can be expressed in components of the body-reference axes O_{B^R} through a sequence of rotations involving these angles and are summarized to coefficient vectors for the aerodynamic forces $\boldsymbol{C}_i^{A,F}|_{B^R}$ and moments $\boldsymbol{C}_i^{A,M}|_{B^R}$, respectively. The resulting forces and moments at either the neutral point (strips) or the center of mass (fuselage) are then given by

$$\boldsymbol{F}_i^A|_{B^R} = \bar{q}_{N,i}\, S_{\mathrm{ref}}\, \boldsymbol{C}_i^{A,F}|_{B^R} \tag{14}$$

$$\boldsymbol{M}_i^A|_{B^R} = \bar{q}_{N,i}\, S_{\mathrm{ref}}\, \boldsymbol{D}\, \boldsymbol{C}_i^{A,M}|_{B^R} \tag{15}$$

with the diagonal matrix $\boldsymbol{D}$, which has the main diagonal elements $\{\bar{s}, \bar{c}, \bar{s}\}$, and the effective dynamic pressures of the normal flow for wing and horizontal tail strips (Eq. 16a) and vertical tail strips (Eq. 16b) as

$$\bar{q}_{N,i} = \bar{q}_{A,i} \cos^2(\beta_{\mathrm{eff},i}) \tag{16a}$$

$$\bar{q}_{N,i} = \bar{q}_{A,i} \cos^2(\alpha_{\mathrm{eff},i}). \tag{16b}$$

The forces and moments of all strips are ultimately transferred to the center of mass and summed up for the equations of motion of the rigid-body degrees of freedom. The generalized forces Q_{η_j} for the equations of the structural dynamics can be obtained by first transferring all strip forces and moments to their respective structure support points. Then, the resulting strip forces and moments are collected in vector form and are subsequently transformed with the transposed mode shapes

$$Q_{\eta_j} = \boldsymbol{\Phi}_j^T \begin{bmatrix} \boldsymbol{F}_x^A \\ \boldsymbol{F}_y^A \\ \boldsymbol{F}_z^A \\ \boldsymbol{M}_x^A \\ \boldsymbol{M}_y^A \\ \boldsymbol{M}_z^A \end{bmatrix}_{SP}. \tag{17}$$

4 Flexible model identification and evaluation

This section is concerned with the identification of the flexible aircraft model and the evaluation of the results. Prior to the actual parameter estimation, a simulation model is assembled and implemented in MATLAB/SIMULINK. Given the equations of motion of the flexible aircraft and the quasi-steady strip aerodynamics model, the model is combined with additional models from the in-house library FLYSIM. These include an earth and atmosphere model, a wind and turbulence model, and an actuator model for the representation of servo and control surface dynamics. Moreover, a propulsion model and landing gear model are added. Subsequently, a suitable set of maneuvers is selected. This is accomplished by post-processing the gathered flight test data and transferring all the available measurement parameters listed in Table 1 to the center of mass. Moreover, the load measurement parameters are corrected by the dead weight of the structure. The selection of maneuvers is based on different criteria, such as precision of maneuver execution, dynamic pressure variations, and atmospheric disturbance.

4.1 Parameter estimation

The estimation of model parameters is performed with the in-house tool DAVIS, using the output error method in the time-domain, as depicted in Fig. 7, and maximum-likelihood estimation [26]. Based on an initial a priori estimation of the model parameters $\boldsymbol{\Theta}_0$, the simulation model is excited by the same inputs $\boldsymbol{u}(t)$ as in the maneuvers of the flight tests (see Sect. 2.3) and the simulated model response $\hat{\boldsymbol{y}}(t)$ is compared to the measured aircraft system response $\boldsymbol{y}(t)$. Only measurement noise $\boldsymbol{v}(t)$ is considered to corrupt the deterministic system output $\boldsymbol{y}_d(t)$. Applying a maximum-likelihood function, the response error $\boldsymbol{y}(t) - \hat{\boldsymbol{y}}(t)$ is minimized in an iterative optimization process through adaption of the model parameters by the parameter change $\Delta\boldsymbol{\Theta}$. To this end, sensitivities ${}^{\partial\hat{\boldsymbol{y}}}/_{\partial\boldsymbol{\Theta}}$ of the model output with respect to the model parameters are calculated.

Suitable model parameters Θ_i to be estimated need to be defined. Since the structural dynamics model was identified

---

[1] Assuming no elastic sweep angle $\varphi_{e,i} = 0$. If $\varphi_{e,i} \neq 0$, a further rotation is given by this angle.

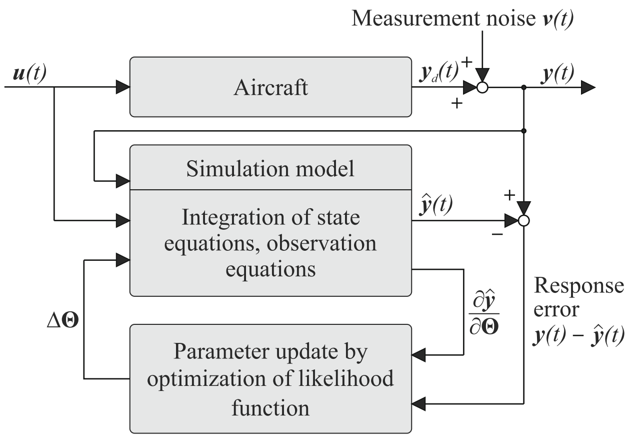

Fig. 7 Block schematic of the output error method with maximum-likelihood function [26]

from GVT data, only parameters of the strip aerodynamics model are estimated. Initial distributions of the normalized stability and control derivatives are obtained from three-dimensional vortex-lattice-method calculations of the aircraft in the open source software tool XFLR5. The aircraft is modeled with its rigid shape lifting surfaces but without fuselage as advised by XFLR5. The influence of lifting surface thickness is neglected and treated as an uncertainty. To this end, all lifting surfaces are divided into spanwise strips based on geometric properties and the resolution of local flow effects. A total number of 48 wing strips, 8 horizontal tail strips, and 5 vertical tail strips are considered. Subsequently, the locations of the strips are used to define associated structure support points as described in Sect. 3.2 and determine the structural mode shapes from the adapted FE-model. The resulting distributions are shown in Fig. 8.

According to the aerodynamic parametrization of the non-dimensional force coefficients, separate distributions are obtained for zero coefficients, stability derivatives, and control derivatives. The associated control surface deflections are $\delta_{a,\text{in}}$ and $\delta_{a,\text{out}}$ for inner and outer ailerons, $\delta_{f,\text{in}}$ and $\delta_{f,\text{out}}$ for inner and outer flaperons, δ_r for the rudder, and δ_e for the elevators. Each wing control surface is assumed to only influence the lift of all strips on the side of the wing it is attached to. Parameters for linearly scaling the initial distributions are introduced and defined as estimation parameters. In this way, the initial distributions can be adapted in the estimation process with a limited number of estimation parameters. On the other hand, the achievable solution is constrained by the qualitative shapes of the initial distributions. Separate scaling parameters are defined for each lifting surface, i.e., wings, horizontal tail, and vertical tail. Scaling parameters for the control derivative distributions of opposite control surfaces are either paired or grouped based on the control allocations used in the flight tests (indicated in Fig. 8 with the color code). The additional stability derivatives of the fuselage and downwash parameters are treated as direct estimation parameters with no effect on the distributions. Stall parameters and k-factors of induced drag are determined separately from flight data and the vortex-lattice-method calculations, respectively, and kept fixed for the estimation. Measurement outputs of the rigid-body motion (center of mass) are selected and set as criteria for the parameter estimation

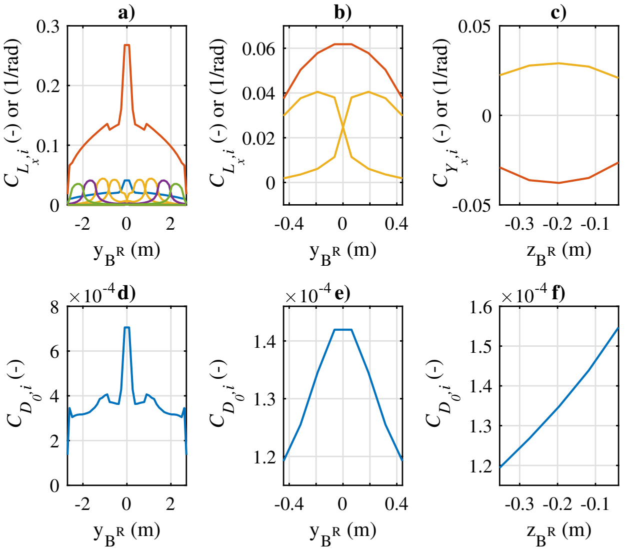

Fig. 8 Initial derivative distributions from XFLR5: a) wing lift with $C_{L_0,i}$ (—), $C_{L_\alpha,i}$ (—), $C_{L_{\delta_f},i}$(—), $C_{L_{\delta_{a,\text{in}}},i}$ (—), $C_{L_{\delta_{a,\text{out}}},i}$ (—), b) horizontal tail lift with $C_{L_\alpha,i}$ (—), $C_{L_{\delta_e},i}$ (—), c) vertical tail side force with $C_{Y_\beta,i}$ (—), $C_{Y_{\delta_r},i}$ (—), d) to f) parasitic drag of wing, horizontal, and vertical tail

$$y = \left[V_{TAS} \ \alpha \ \beta \ \dot{p} \ \dot{q} \ \dot{r} \ p \ q \ r \ \Phi \ \Theta \ \Psi \ a_x \ a_y \ a_z \ u \ v \ w \right]^T . \tag{18}$$

Herein, V_{TAS}, α, and β are the true airspeed, angle of attack, and angle of sideslip, p, q, and r the roll, pitch, and yaw rates, Φ, Θ, and Ψ are the Euler angles for roll, pitch, and yaw, and u, v, and w are the translational velocities expressed on O_{BR} coordinates.

The values and relative standard deviations of the final estimated distribution scaling parameters are listed in Table 3. A value close to 1 indicates an estimation result close to the initial distributions from XFLR5. This is found for the parameter $k\_C_{Y_\beta}$ of the vertical tail, the parameters $k\_C_{L_\alpha,\text{wing}}$ and $k\_C_{L_\alpha,\text{htp}}$ of the wing and the horizontal tail, and the parameter $k\_C_{L_{\delta_{a,\text{out}}}}$ of the outer ailerons. Least agreement with the initial distributions from XFLR5 are found for the parameters $k\_C_{D_0}$ of all lifting surfaces, $k\_C_{L_0,\text{wing}}$ of the wing, and $k\_C_{L_{\delta_e}}$ of the elevators. The result of $k\_C_{D_0}$ being significantly underestimated by XFLR5 is expected considering the interpolation of viscous drag from two-dimensional polar data associated with the calculation method. Low relative

Table 3 Estimated distribution scaling parameters

Θ_i	Value	Rel. std. deviation (%)
$k\_C_{D_0}$	3.1389	1.95
$k\_C_{Y_\beta}$	0.9988	0.82
$k\_C_{Y_{\delta_r}}$	0.8234	1.33
$k\_C_{L_0,\text{wing}}$	0.3105	3.26
$k\_C_{L_\alpha,\text{wing}}$	1.1425	0.87
$k\_C_{L_\alpha,\text{htp}}$	0.8897	0.76
$k\_C_{L_{\delta_f}}$	0.7746	1.09
$k\_C_{L_{\delta_e}}$	0.5646	0.74
$k\_C_{L_{\delta_{a,\text{in}}}}$	0.7401	1.08
$k\_C_{L_{\delta_{a,\text{out}}}}$	0.9731	0.99

Table 4 Estimated additional parameters

Θ_i	Value	Rel. std. deviation (%)
${}^{\partial\epsilon_T}/_{\partial\alpha}$	0.411	1.75
${}^{\partial\epsilon_T}/_{\partial\delta_f}$	0.0248	1.72
$C_{Y_{\beta,\text{fuse}}}$	−0.1295	11.82
$C_{l_{0,\text{fuse}}}$	−0.0017	1.01
$C_{m_{0,\text{fuse}}}$	−0.0378	4.87

standard deviations are achieved for all estimated distribution scaling parameters.

Table 4 further lists the values and relative standard deviations of the final estimated additional parameters of the fuselage and downwash. Only a few parameters for the most dominant fuselage effects are incorporated in the final parameter set. An increased relative standard deviation is only observed for the parameter $C_{Y_{\beta,\text{fuse}}}$ of the fuselage.

Matching plots of the identification result are shown in Fig. 9 for longitudinal and lateral maneuvers with measurement parameters at the center of mass. A good overall identification result is achieved for all maneuvers. Especially, the fast aircraft dynamics are matched well, which is important for control law design. Good matches are also achieved for the translational rigid-body accelerations (a_x, a_y, a_z), which are directly related to the external forces acting on the aircraft. Note that gravitational accelerations are not measured by the sensors. Some model deficiencies are found for the measurement parameters true airspeed V_{TAS} and pitch angle Θ, which indicate slight deviations of the model's pitching moment to the measured aircraft's pitching moment. Unexpected model behavior is also observed in the last part of the level deceleration maneuver. However, judging from the control action of ailerons and rudder, an undetected asymmetric atmospheric disturbance is suspected to influence the maneuver.

Table 5 Theil's inequality coefficient of the identification result

Measurement parameter	Symbol	U_i
Altitude	h	0.050
True airspeed	V_{TAS}	0.268
Roll angle	Φ	0.190
Pitch angle	Θ	0.215
Angle of attack	α	0.277
Angle of sideslip	β	0.160
Roll rate	p	0.183
Pitch rate	q	0.192
Yaw rate	r	0.168
Longitudinal acceleration	a_x	0.292
Lateral acceleration	a_y	0.263
Vertical acceleration	a_z	0.193

The identification result is further analyzed by means of Theil's inequality coefficient (TIC) [32]. First introduced in the field of economics, the coefficient provides a measure of the accuracy of a prediction from a model with its value ranging from zero to unity. Due to its simplicity, it is often adopted for system identification (e.g., [20]). The Theil's inequality coefficient U_i is defined as

$$U_i = \frac{\sqrt{\frac{1}{N}\sum_{k=1}^{N}(y_i(t_k) - \hat{y}_i(t_k))^2}}{\sqrt{\frac{1}{N}\sum_{k=1}^{N}(y_i(t_k))^2} + \sqrt{\frac{1}{N}\sum_{k=1}^{N}(\hat{y}_i(t_k))^2}}, \tag{19}$$

with N denoting the number of samples, and $y_i(t_k)$ and $\hat{y}_i(t_k)$), as previously defined, denoting the measured aircraft system response and simulated model response, respectively. However, in the calculation of the coefficient, these outputs are implemented as the variations from the initial condition $y_i(t_{\text{init}})$ [33]. In the present case of a sequence of multiple maneuvers, the initial condition of each individual maneuver has to be used. Table 5 lists the Theil's inequality coefficient for all measurement parameters of the identification result in Fig. 9. A value of zero corresponds to a perfect model prediction, whereas values close to unity indicate significantly different responses. Values below 0.3 are said to indicate a good agreement of measured and simulated responses [34]. As can be seen from Table 5, this is the case for all measurement parameters. The differences in TIC values further confirm the visual impression of the identification result in Fig. 9.

4.2 Evaluation of structural load distribution

In a final step, the identified model is evaluated with regard to its capability to estimate distributed structural loads and its use in active load control law design. To this end, struc-

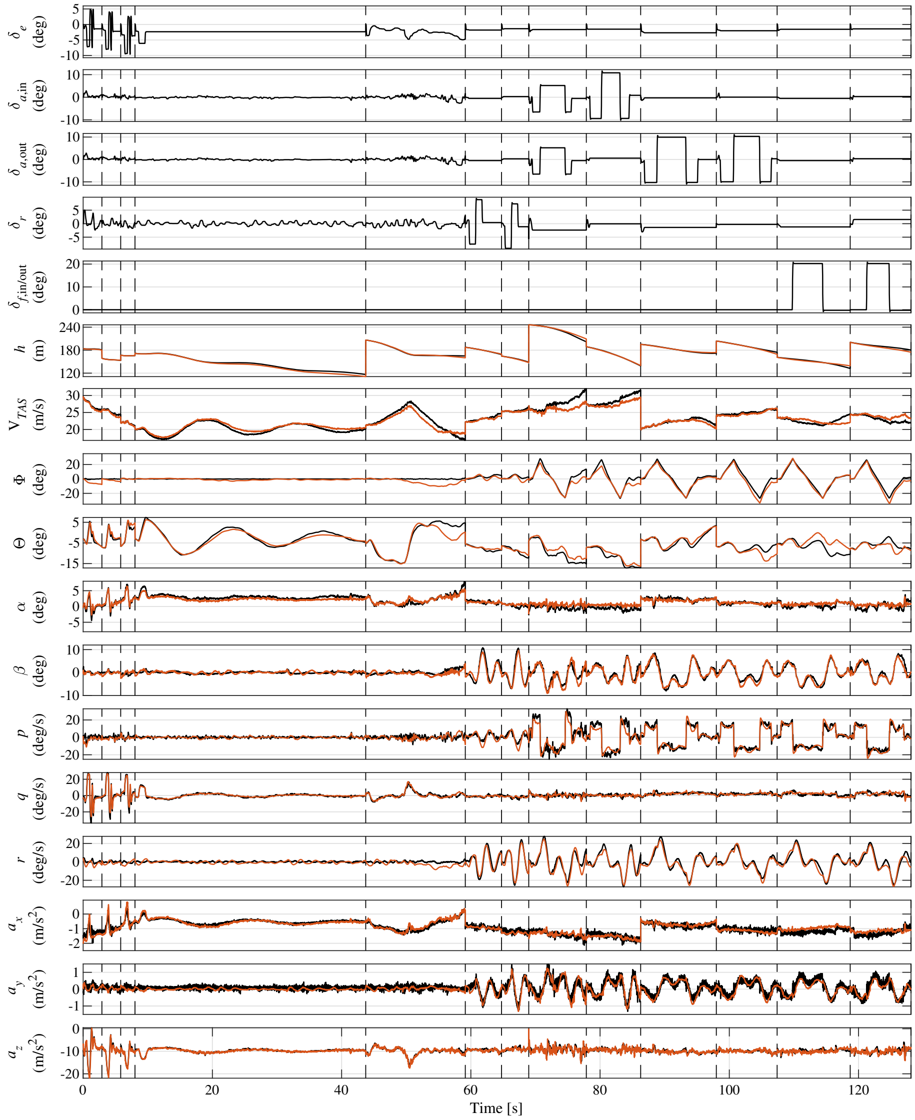

Fig. 9 Identification result for longitudinal/lateral maneuvers with measurement parameters at the center of mass, measurement (—), simulation (—), and maneuver separation (– –)

tural loads measured at wing load measurement stations are compared to the model outputs. The outputs are constructed as part of a separate loads model and capture the internal loads acting on the strain gauges of the load measurement stations. Aerodynamic forces and moments as well as inertial forces at local mass points (MP) are considered. The mass points are defined based on the locations of the strain gauges and a detailed CAD model. The aerodynamic strip forces and moments are allocated and transferred to these mass points considering their elastic points of attack. Elastic position vectors of the mass points can be obtained similar to Eq. 8 and an interpolation of mode shapes $\boldsymbol{\Phi}_j(x, y, z)$ at the mass point positions, assuming a rigid connection between mass point and elastic axis. Next, inertial forces are added. Local accelerations are derived based on [35] which include rigid-body accelerations and the effects of elastic deformation on angular rates and translational acceleration. The total forces and moments at the mass points $\boldsymbol{F}_{\text{MP}_i} = [F_x \; F_y \; F_z \; M_x \; M_y \; M_z]^T$ are then used to calculate the internal loads $\boldsymbol{F}_{\text{SG}_i} = [Q_x \; Q_y \; Q_z \; M_x \; M_y \; M_z]^T$ by transferring them to the strain gauge positions. Figure 10 exemplifies the internal loads at SG$_{10}$ on the right wing.

For the single pair of MP$_{10}$ and SG$_{10}$ with individual distance $[\Delta x, \Delta y, \Delta z]$ from mass point to strain gauge along the axes of O_{B^R}, the internal loads at SG$_{10}$ due to the forces and moments at MP$_{10}$ can be derived according to [36, 37] as

$$\begin{bmatrix} Q_x \\ Q_y \\ Q_z \\ M_x \\ M_y \\ M_z \end{bmatrix}_{\text{SG}_{10}} = \begin{bmatrix} 1 & 0 & 0 & 0 & 0 & 0 \\ 0 & 1 & 0 & 0 & 0 & 0 \\ 0 & 0 & 1 & 0 & 0 & 0 \\ 0 & -\Delta z & \Delta y & 1 & 0 & 0 \\ \Delta z & 0 & -\Delta x & 0 & 1 & 0 \\ -\Delta y & \Delta x & 0 & 0 & 0 & 1 \end{bmatrix} \cdot \begin{bmatrix} F_x \\ F_y \\ F_z \\ M_x \\ M_y \\ M_z \end{bmatrix}_{\text{MP}_{10}} \tag{20}$$

$$\boldsymbol{F}_{\text{SG}_{10}} = \boldsymbol{T}_{\text{SG}_{10}\text{MP}_{10}} \cdot \boldsymbol{F}_{\text{MP}_{10}}. \tag{21}$$

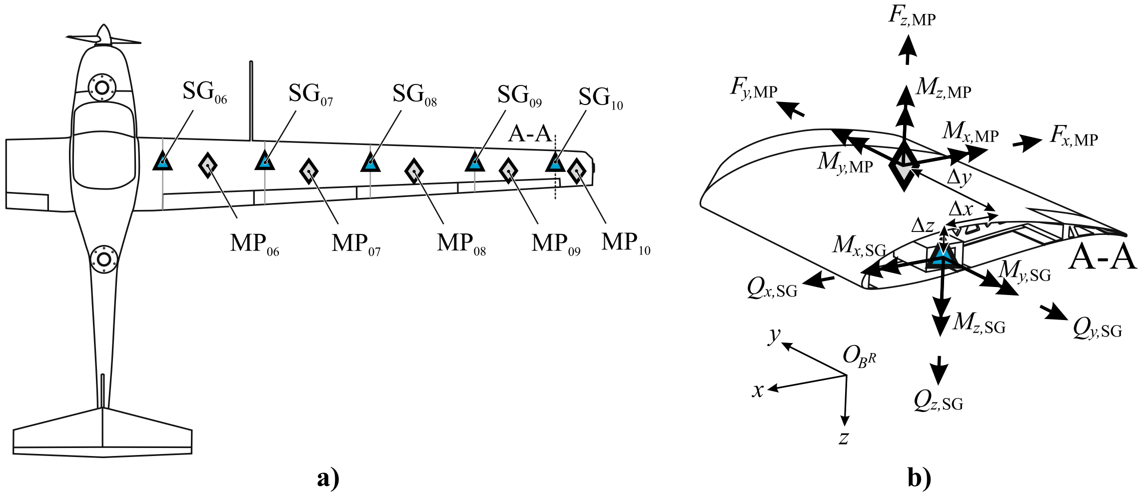

Fig. 10 Calculation of internal loads in O_{B^R}: a) position of strain gauges (SG) and mass points (MP) on the right wing; b) sum of forces and moments at SG_{10} (section A–A)

Similarly, the internal loads from other pairs of mass points and strain gauges can be calculated, each by applying the respective distance from mass point to strain gauge. For the total internal loads at all strain gauges on the right wing, a total transformation matrix can be constructed with each of the transformation matrices corresponding to single pairs of mass points and strain gauges, as shown in Eq. 20, to

$$\begin{bmatrix} \boldsymbol{F}_{\mathrm{SG}_{10}} \\ \boldsymbol{F}_{\mathrm{SG}_{09}} \\ \boldsymbol{F}_{\mathrm{SG}_{08}} \\ \boldsymbol{F}_{\mathrm{SG}_{07}} \\ \boldsymbol{F}_{\mathrm{SG}_{06}} \end{bmatrix} = \begin{bmatrix} \boldsymbol{T}_{\mathrm{SG}_{10}\mathrm{MP}_{10}} & 0 & \cdots & 0 \\ \boldsymbol{T}_{\mathrm{SG}_{09}\mathrm{MP}_{10}} & \boldsymbol{T}_{\mathrm{SG}_{09}\mathrm{MP}_{09}} & \cdots & 0 \\ \boldsymbol{T}_{\mathrm{SG}_{08}\mathrm{MP}_{10}} & \boldsymbol{T}_{\mathrm{SG}_{08}\mathrm{MP}_{09}} & \cdots & 0 \\ \boldsymbol{T}_{\mathrm{SG}_{07}\mathrm{MP}_{10}} & \boldsymbol{T}_{\mathrm{SG}_{07}\mathrm{MP}_{09}} & \cdots & 0 \\ \boldsymbol{T}_{\mathrm{SG}_{06}\mathrm{MP}_{10}} & \boldsymbol{T}_{\mathrm{SG}_{06}\mathrm{MP}_{09}} & \cdots & \boldsymbol{T}_{\mathrm{SG}_{06}\mathrm{MP}_{06}} \end{bmatrix} \cdot \begin{bmatrix} \boldsymbol{F}_{\mathrm{MP}_{10}} \\ \boldsymbol{F}_{\mathrm{MP}_{09}} \\ \vdots \\ \boldsymbol{F}_{\mathrm{MP}_{06}} \end{bmatrix}. \quad (22)$$

As seen in the equation, the forces and moments at all mass points MP_6 to MP_{10} contribute to the total internal loads at the innermost strain gauge SG_6.

With Eq. 22, the internal loads at the strain gauges are given in components of O_{B^R} which is compliant with the calibration axes of the sensors on the G-Flights Dimona. However, if the calibration is given in the sensor coordinate systems $O_{B^{SG_i}}$, in a final step, the internal loads need to be transformed into the sensor coordinate systems with the transformation matrices $\boldsymbol{T}_{B^{SG_i}B^R}$. The rotation angles are then given by the sum of rigid-body and elastic angular deformation angles at the sensor positions relative to O_{B^R}. The latter can be determined through an interpolation of mode shapes for elastic angular deformation $\boldsymbol{\Phi}_{\mathrm{ang},j}(x, y, z)$ at the sensor positions and generalized displacement coordinates $\eta_j(t)$. The same overall approach is used to calculate the internal loads at the strain gauges on the left wing and empennage.

Figure 11 compares the shear forces Q_z measured at middle and inner load measurement stations along the wing (see Fig. 2) to the respective outputs of the structural loads' model for the same maneuver sequence.

Close matches are found for all shear forces for the majority of maneuvers. This result indicates a plausible representation of the actual load distribution along the wing. Moreover, the close match of shear forces at inner load measurement stations $Q_{z,\mathrm{LMS5}}$ (left wing) and $Q_{z,\mathrm{LMS6}}$ (right wing) is in good agreement with the identification result of a_z, since both stations capture the majority of aerodynamic loads. An unexpected model behavior is solely found for the inner load measurement stations during flaperon bank-to-bank maneuvers, where the effects of local load increase/decrease due to flaperon deflection and the resulting rotation of the aircraft are not represented correctly. It is suspected that either the negligence of a dedicated fuselage model within XFLR5 and therewith negligence of wing–fuselage interaction effects on the initial derivative distributions, or the load application on the inner load measurement stations is a possible cause of the deviation.

Three-dimensional effects on the induced angle of attack were investigated in [38] with a 1 g and 2.5g wind tunnel wing shape and were found to cause deviations in the sectional aerodynamic loads if not properly modeled. The effects were observed to be approximately proportional to the wing's elastic twist. With the initial derivative distributions being derived from three-dimensional vortex lattice method calculations of the rigid aircraft shape only, these effects are not accounted for and thus add to the uncertainty of the results. However, considering the moderate magnitudes of elastic twist experienced during the maneuvers and the plausible load distributions found from the evaluation of shear forces in Fig. 11, this uncertainty is considered small. If more aggressive maneuvers or gust encounters with larger elastic deformations and increased elastic mode participation are

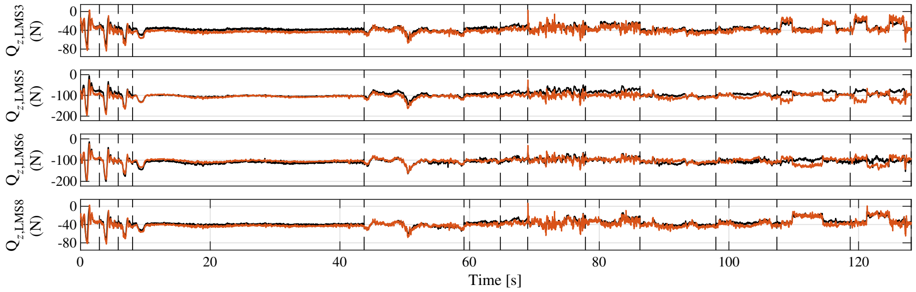

Fig. 11 Identification result for longitudinal/lateral maneuvers with measured shear forces on the wing, measurement (—), simulation (—), and maneuver separation (– –)

to be investigated in the future, the influence of the three-dimensional effects on the induced angle of attack is expected to increase. In this case, even unsteady aerodynamic effects can become important for slightly flexible aircraft as represented by the G-Flights Dimona [13].

Based on these results, the identified model is capable of computing realistic distributed aerodynamic forces and moments and thus is well suited for state of the art model-based load estimation techniques [36]. This aspect combined with the simple model structure also provides a suitable basis for real-time simulation and the design of active load control laws.

5 Conclusion

A control-oriented modeling framework for slightly flexible aircraft suitable for parameter identification in the time-domain was presented. It combines linear structural dynamics and a distributed quasi-steady aerodynamics model using strip theory. The applicability of the modeling framework was demonstrated for a slightly flexible 25 kg fixed-wing UAV. Free vibration modes and mode shapes of the structure were obtained from ground vibration tests. Initial distributions for the stability and control derivatives of the strip aerodynamics were derived from three-dimensional vortex-lattice-method steady-flow calculations. They were subsequently adapted based on flight test data using the output error method in the time-domain and maximum-likelihood estimation. The use of scaling parameters for adapting the initial distributions is demonstrated to be an efficient approach for achieving a limited number of estimation parameters. A good overall identification result and close match of the fast aircraft dynamics was achieved. Good agreement with the initial derivative distributions was found for the lift curve slope and angle of sideslip-dependent stability derivative distributions, while viscous drag effects were significantly underestimated by the vortex-lattice-method calculations. Further, the evaluation of the structural load distribution measured along the wing demonstrated the capability of the model to compute realistic distributed aerodynamic forces and moments. The resultant computationally efficient model provides a suitable basis for real-time simulation, loads' estimation, and active load control law design. The latter highly benefit from the capability of the strip aerodynamic model structure to yield distributed forces and moments. Possible future work includes the improvement of the derivative distributions based on high-fidelity numerical or experimental data.

Acknowledgements The authors would like to acknowledge Lothar Desel and Rasmus Köhler for their support during the flight test campaign. Special thanks is further devoted to Karsten Henning for his contribution to this work. Parts of this work have been presented previously at the 6th CEAS Conference on Guidance, Navigation and Control (EuroGNC) [39].

Funding Open Access funding enabled and organized by Projekt DEAL. This work was funded by the research project "Advanced load analysis and observer methods for innovative aircraft configurations" (ELASTIK), which is supported by the German Federal Ministry for Economic Affairs and Climate Action in the national LuFo V-3 program. Any opinions, findings, and conclusions expressed in this document are those of the authors and do not necessarily reflect the views of the other project partners.

Availability of data and materials Not applicable.

Declarations

Conflict of interest The authors have no competing interests to declare that are relevant to the content of this article.

Ethics approval Not applicable.

Consent to participate Not applicable.

Consent for publication Not applicable.

Code availability Not applicable.

References

1. Livne, E.: Future of airplane aeroelasticity. J. Aircraft **40**(6), 1066–1092 (2003). https://doi.org/10.2514/2.7218
2. Waszak, M.R., Davidson, J.B., Schmidt, D.K.: A simulation study of the flight dynamics of elastic aircraft. Technical Report NASA CR 4102 Vols. 1 and 2, NASA (1987)
3. Kubica, F.: New flight control laws for large capacity aircraft experimentation of Airbus A340. In: ICAS, Congress, 21st, Melbourne, Australia (1998)
4. Tuzcu, I., Meirovitch, L.: Effects of flexibility on the stability of flying aircraft. J. Dyn. Syst. Meas. Contr. **127**(1), 41–49 (2004). https://doi.org/10.1115/1.1870040
5. Jategaonkar, R., Fischenberg, D., von Gruenhagen, W.: Aerodynamic modeling and system identification from flight data-recent applications at DLR **41**(4), 681–691 (2004). https://doi.org/10.2514/1.3165
6. Waszak, M.R., Schmidt, D.K.: Flight dynamics of aeroelastic vehicles **25**(6), 563–571 (1988). https://doi.org/10.2514/3.45623
7. Schmidt, D.K., Raney, D.L.: Modeling and simulation of flexible flight vehicles. J. Guid. Control. Dyn. **24**(3), 539–546 (2001). https://doi.org/10.2514/2.4744
8. Pete, K., Smith, S., Vicroy, D.: Model validation for wake-vortex/aircraft encounters. In: AIAA Atmospheric Flight Mechanics Conference. American Institute of Aeronautics and Astronautics, Denver, Colorado (2000). https://doi.org/10.2514/6.2000-3979
9. De Bruin, A.: S-wake assessment of wake vortex safety. National Aerospace Laboratory NLR (2003)
10. Fischenberg, D.: A method to validate wake vortex encounter models from flight test data. In: 27th International Congress of the Aeronautical Sciences (2010). International Council of the Aeronautical Sciences Nice, France
11. Selig, M.: Modeling full-envelope aerodynamics of small UAVs in realtime. In: AIAA Atmospheric Flight Mechanics Conference. American Institute of Aeronautics and Astronautics, Toronto, Ontario, Canada (2010). https://doi.org/10.2514/6.2010-7635
12. Silvestre, F., Paglione, P.: Dynamics and control of a flexible aircraft. In: AIAA Atmospheric Flight Mechanics Conference and Exhibit. American Institute of Aeronautics and Astronautics, Honolulu, Hawaii (2008). https://doi.org/10.2514/6.2008-6876
13. Silvestre, F.J., Luckner, R.: Experimental validation of a flight simulation model for slightly flexible aircraft **53**(12), 3620–3636 (2015). https://doi.org/10.2514/1.j054023
14. Andrews, S.: Modelling and simulation of flexible aircraft : handling qualities with active load control. PhD thesis (2011)
15. Yates, E.C.: Modified-strip-analysis method for predicting wing flutter at subsonic to hypersonic speeds. J. Aircr. **3**(1), 25–29 (1966). https://doi.org/10.2514/3.43702
16. Weissinger, J.: The lift distribution of swept-back wings. Technical Report NACA-TN-1120, National Advisory Committee for Aeronautics (1947)
17. Wagner, H.: Über die Entstehung des dynamischen Auftriebes von Tragflügeln. ZAMM - Zeitschrift für Angewandte Mathematik und Mechanik **5**(1), 17–35 (1925). https://doi.org/10.1002/zamm.19250050103
18. Leishman, J.G.: Unsteady lift of a flapped airfoil by indicial concepts. J. Aircr. **31**(2), 288–297 (1994). https://doi.org/10.2514/3.46486
19. de Oliveira Silva, B.G.: Data gathering and preliminary results of the system identification of a flexible aircraft model. In: AIAA Atmospheric Flight Mechanics Conference. American Institute of Aeronautics and Astronautics, Portland, Oregon (2011). https://doi.org/10.2514/6.2011-6355
20. de Oliveira Silva, B.G., Moennich, W.: System identification of flexible aircraft in time domain. In: AIAA Atmospheric Flight Mechanics Conference. American Institute of Aeronautics and Astronautics, Minneapolis, Minnesota (2012). https://doi.org/10.2514/6.2012-4412
21. Garrec, C.L., Kubica, F.: In-flight structural modes identification for comfort improvement by flight control laws **42**(1), 90–92 (2005). https://doi.org/10.2514/1.3733
22. Niemann, C., Montel, M., Thielecke, F.: Development of an air data system for an unmanned research aircraft. In: Deutscher Luft-und Raumfahrtkongress (2014)
23. Henning, K., Montel, M., Thielecke, F.: Experimentelle Ermittlung der modalen Strukturparameter eines skalierten Flugversuchstraegers mittels Low-Cost Sensoren. In: Deutscher Luft- und Raumfahrtkongress DLRK, Muenchen, Germany (2017)
24. Krings, M., Henning, K., Thielecke, F.: Flight test oriented autopilot design for improved aerodynamic parameter identification. In: Advances in Aerospace Guidance. Navigation and Control, pp. 265–276. Springer, Berlin (2013)
25. Krings, M., Annighoefer, B., Thielecke, F.: Ultra - unmanned low-cost testing research aircraft. In: American Control Conference ACC (2013)
26. Jategaonkar, R.: Flight Vehicle System Identification?: a Time Domain Methodology. American Institute of Aeronautics and Astronautics, Reston, Virginia (2006)
27. Keyes, S.A., Seiler, P., Schmidt, D.K.: Newtonian development of the mean-axis reference frame for flexible aircraft. J. Aircr. **56**(1), 392–397 (2019). https://doi.org/10.2514/1.c035041
28. Milne, R.D.: Dynamics of the deformable aeroplane. Technical report, Aeronautical Research Council London (United Kingdom) (1964)
29. Canavin, J.R., Likins, P.W.: Floating reference frames for flexible spacecraft. J. Spacecr. Rocket. **14**(12), 724–732 (1977). https://doi.org/10.2514/3.57256
30. Schlichting, H., Truckenbrodt, E.: Aerodynamik des Flugzeuges: Zweiter Band. Springer, Berlin (1960). https://doi.org/10.1007/978-3-642-53046-3
31. Brockhaus, R., Alles, W., Luckner, R.: Flugregelung. Springer, Berlin (2011). https://doi.org/10.1007/978-3-642-01443-7
32. Theil, H.: Economic Forecasts and Policy, 2nd edn. Contributions to economic analysis. North-Holland Publishing Company, Amsterdam (1975)
33. Leuthold, R.M.: On the use of theil's inequality coefficients. Am. J. Agr. Econ. **57**(2), 344–346 (1975). https://doi.org/10.2307/1238512
34. Murray-Smith, D.J.: Methods for the external validation of contiuous system simulation models:a review. Math. Comput. Model. Dyn. Syst. **4**(1), 5–31 (1998). https://doi.org/10.1080/13873959808837066
35. Grauer, J.A., Boucher, M.J.: Output measurement equations for flexible aircraft flight dynamics. Technical Report No. NASA/TM-2018-220102, NASA STI Program Office (2018)
36. Montel, M., Thielecke, F.: Efficient and accurate technology for aircraft loads estimation. CEAS Aeronaut. J. **11**(2), 461–474 (2019). https://doi.org/10.1007/s13272-019-00423-z
37. Luderer, O., Thielecke, F.: Validation of a hybrid loads observer for a subscale test aircraft with distributed electric propulsion. In: 33rd Congress of the International Council of the Aeronautical Sciences, ICAS 2022, Stockholm, Sweden (2022). International Council of the Aeronautical Sciences (ICAS). http://hdl.handle.net/11420/14391
38. Barriety, B., Boin, J.-P., Chandre-Vila, O., Mauermann, T.: Fast fluid-structure computational method taking into account non-

linear aerodynamic. In: International Forum on Aeroelasticity and Structural Dynamics (IFASD) (2019)

39. Herrmann, B., Theis, J., Thielecke, F.: System Identification of a Nonlinear UAV Model with Distributed Aerodynamics and Flexible Structure. In: 6th Conference on Guidance, Navigation and Control CEAS (2022)